Refractive index structure function coefficient calculation and classification based on radiosonde and ground-based observation.

Bryan I. Mendoza[1], Christopher MN Cicalla[2], Daniel V. Foti[3]
Department of Mechanical Engineering, University of Memphis, Memphis, Tennessee, 38152, United States of America

I. Abstract

The computation of the optical refractive index structure function coefficient, Cn2, using the Tatarskii-based model is crucial for assessing scintillation intensity, a critical factor for ground-based optical astronomy instruments. However, obtaining necessary atmospheric conditions at desired spatial-temporal resolution is infeasible, so simplifying the assumption of homogeneity and isotropy are often applied. In this work, we incorporate meteorological observations obtained at the Department of Energy Atmospheric Radiation Measurement user facility at the Southern Great Plains. Radiosonde and land-based eddy covariance station data are used to correlate temperatures and pressures with altitude and atmospheric stability. A method to calculate C_n^2 [Quatresooz, et al, Radio Science, 58, 2023] from radiosonde temperature and pressure is classified and assess based on stability. The computed C_n^2exhibits a noticeable alignment with results from previous works using data from other locations but does not vary significantly with atmospheric stability based on the Monin-Okobuv length in the upper atmosphere.

II. Nomenclature

p = pressure

T = temperature

C_{n^2} = optical refractive index structure parameter

Δz = vertical spacing used for resampling data

n = refractive index

$n_0[i]$ = mean refractive index

ω = window size used for the computation of the mean refractive index

n_i = fluctuations within refractive index

δ = ($m\Delta$z) The vertical spacing component used to compute the average C_n^2

III. Introduction

Driving down the road and noticing “heat waves” and or noticing the stars twinkling in the nighttime sky share the same obstacles that ground-based astronomy and Earth-to-satellite communication have. Optical turbulence is the effect of random fluctuations that occur due to atmospheric turbulence. As a plane travels across the sky, the jostle

Undergraduate, Department of Mechanical Engineering, Student Member Bryan Mendoza (1400317)
Undergraduate, Department of Mechanical Engineering, Student Member Christopher Cicalla (1603493)
Faculty, Department of Mechanical Engineering, Member Daniel Foti (450024)

and bumps of turbulence are the same reason there is something in the desert, but behind the phenomenon that was never there.

Fluctuations in the refractive index of the Earth's atmosphere are created by wind blowing across the surface and the temperature from ground level up. This is a leading cause of laser beam wandering and spread. This phenomenon does not affect just lasers, the human eye, telescopes, air-based conveyances, and more. The tiny unseen disturbances, eddies low- and high-pressure bubbles, disrupt and alter the path of the laser.

Using the C_n^2 data from the Southern Great Plains facility of the Department of Energy atmospheric radiation measurements, April 1, 2022 – April 1, 2023. Once the profiles were generated, they were used to compare the Quatresooz et. Al paper was done in Trappes, France as well as Hilo, Hawaii since the data and graphs were there.

IV. Experimental Methodology for the C_n^2

We pulled the radiosonde data from the Department of Energy Atmospheric Radiation Measurement facility user the Southern Great Plains (SPG) to make observations at different atmospheric levels. Once gathered it needed to be oriented to a fit model so it could be calculated and then divided into the classification of very stable, stable, neutral stable, neutral, neutral unstable, unstable, very unstable.

First there is the interpolation of the data. Here the interpolation could be set to a distance based on the data acquisition rate i.e., a distance $\Delta z = 5$ meters or less data when $\Delta z = 100$ meters or greater. Using $\Delta z = 25$ meters was used based on previous work. Using the pressures (p) and temperatures (T), at $\Delta z = 25$, and we obtained the refractive index from Eqn. (1). A mean refractive index is then evaluated using Eq. (2). Then any fluctuations can be obtained using Eqn. (3), $n_1 = n - n_0$. From there the following Tatarskii-based model [Quatresooz, et al, Radio Science, 58, 2023] Eq. (4), is used to get a C_n^2 model that can be applied to get the profiles. The refractive index is obtained from

$$n = 1 + 79 \times 10^6 \left(\frac{p}{T} \right) \quad (1)$$

In Eq. (1), p is the pressure from the sonde data is measured in hectopascal (hPa) and the temperature, T, is measured in degrees Celsius (°C).

$$n_0[i] = \frac{\sum_{j=-\omega}^{\omega} n[j]}{2\omega + 1} \quad (2)$$

Here the mean refractive index n_0 is computed using $\omega = 3$

$$n_1 = n - n_0 \quad (3)$$

Equation (3) is used to obtain fluctuations within the refractive indexes. Where n_0 is the mean refractive index from the previous equation Eq. (2)

$$C_n^2(z) = \frac{1}{c\,\Delta z} \frac{(n_1(z+\delta) - n_1(z))^2 + (n_1(z) - n_1(z-\delta))^2}{2\,\delta^{2/3}} \quad (4)$$

Equation (4) depicts the Tatarskii-based model to compute the corresponding optical refractive index parameters.

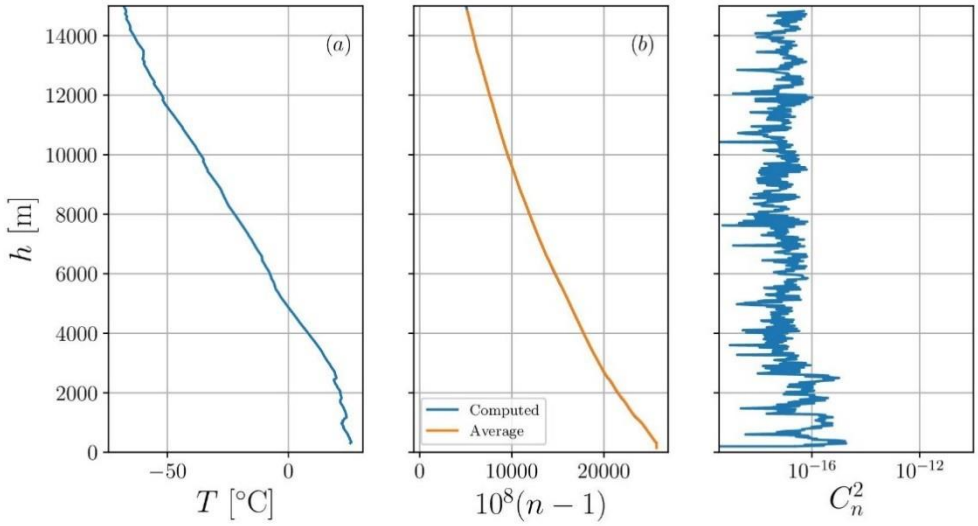

Fig. 1 Single instance of radiosonde observation starting near ground and up to 14km on June 15, 2022, at 11:30 am showing (a) *vertical temperature profile.* (b) *average refractive index calculated from radiosonde pressure and temperature, and (*c) *computed C_n^2 based on the described methodology*

V. Results

Radiosonde observations are collected over one year from April 2022 to April 2023 at the SPG site. A radiosonde observation is launched routinely several times a day. To start, we focus on the observations from June 15, 2023. Figure 1(a) shows the vertical temperature profile with altitude starting at through ground and up to 14 km. Within the first 2000 m from the ground, the radiosonde is traversing the atmospheric boundary layer and the temperature changes relatively little. There are temperature fluctuations indicating that the boundary layer stability is changing now. Above the boundary layer, the temperature decreases linearly across the freezing point and continues to decrease on the radiosonde ascent. Figure 1(b) shows the average refractive index of air calculated from the radiosonde pressure and temperature using Eq. (1).

Overall, the refractive index decreases with height due to the changes in the pressure and temperature. Figure 1(c) shows the computed structure function coefficient, C_n^2 based on the methodology described above. While there are significant fluctuations, on average it is slightly lower than 1 x 10^{-16}, which is relatively low but consistent with Quatresooz, et al. Within the atmospheric boundary layer (first ~2000 m), the coefficient is higher due to larger fluctuations, higher temperature, higher pressure, and the effects of rising air from the ground temperature. However, the profiles are noisy, due to the small average sample size because here we focused on a single observation.

The radiosonde is launched near a meteorological tower equipped with an eddy correlation station that can compute the turbulent, sensible heat, and latent heat fluxes from wind and ground measurements. The fluxes are continuously acquired over 30-minute periods corresponding to 48 measurements daily. The met tower data is selected for each radiosonde launch where the mean wind speed was greater than 3 m/s to ensure that the shear in the boundary layer was adequately high. The average ground data provides information about the conditions at the ground where the radiosonde does not observe. One of the important observations of the met tower data is the ability to assess the boundary layer stability.

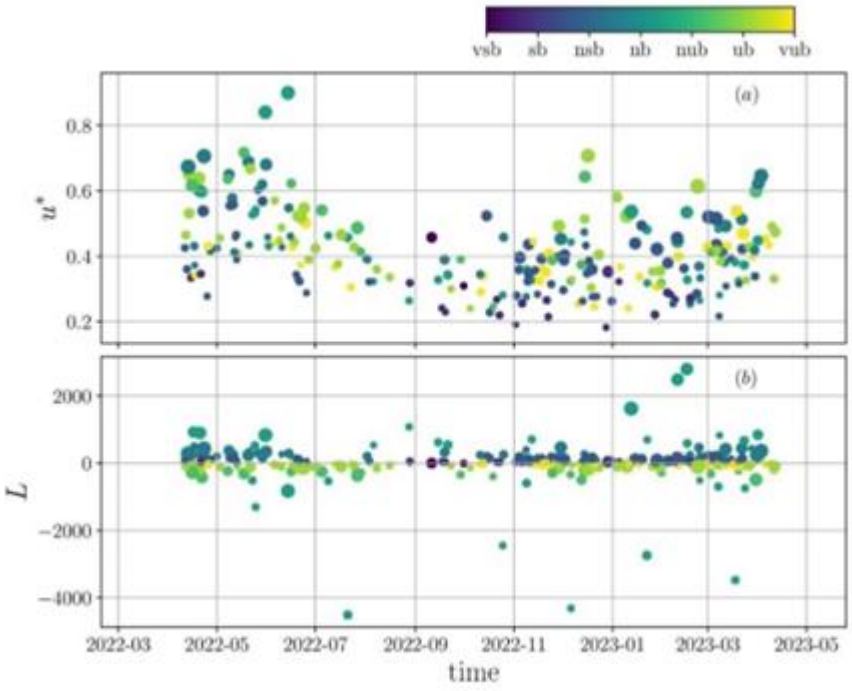

Fig. 2 Thirty-minute averaged observations from met tower at 4m from April 2022 to April 2023 with (a) the friction velocity and (b) the Monin-Obukhov length scale during radiosonde launches. The color of the markers corresponds to the stability regime, and the size of the marker is proportional to the mean wind speed squared.

Figure 2 shows the ground observations from the met tower at 4m height processed at the eddy correlation station with statistics based on 30-minute averages. Ground observations are continuously collected, but radiosondes are only launched at scheduled times. We focus on the 30-min averaged met tower that is observed during the radiosonde ascent. Fig. 2 (a) shows the friction velocity related to the turbulent shear stress at the ground. There is a broad range of friction velocities. Note that the highest friction velocity is often associated with a higher mean wind speed. The size of the marker is related to the kinetic energy ($\mathbf{U}^2_{wind}$). However, stability is not shown to be a direct relationship. The coloring in Fig. 2 is based on the stability criteria for the Monin-Okobhov similar hypothesis. There are seven different stability classifications:

Very Stable (vsb)	$50 > \boldsymbol{L} > 10$
Stable(sb)	$200 > \boldsymbol{L} > 50$
Neutrally Stable (nsb)	$500 > \boldsymbol{L} > 200$
Neutral (nb)	$\lvert \boldsymbol{L} \rvert > 500$
Neutrally Unstable (nub)	$-500 > \mathbf{L} > -200$
Unstable (ub)	$-200 > \mathbf{L} > -50$
Very Unstable (vub)	$-50 > \mathbf{L} > -10$

To track stability, we needed to see the temperature variation and friction velocities. We used u^* to measure the friction velocities and T^* as a temperature scaler. This allowed us to see there is a trend with temperature and stability. Readings with a high u^* value correlate with a higher friction velocity resulting in more turbulence (shear flow). Since an identifiable trend fails to appear, the recorded u^* is in no manner related to stability. The Monin-Obukhov Length (L) as h is the relationship that as height at which turbulence is generated more by buoyancy that wind shear forces.

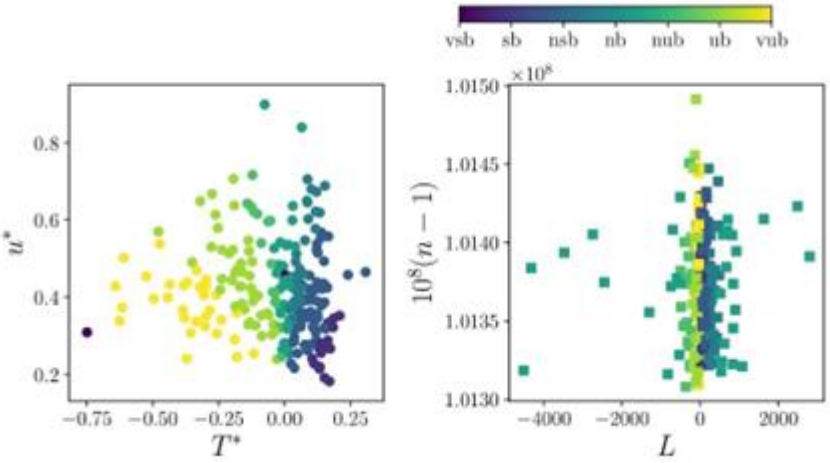

Fig. 3 Stability displayed with (a) *u in relation to *T** and (b) the refractive index in relation to the Monin-Obukhov Length**

Figure 3(a) compares the friction velocity and the scaling temperature, the temperature scale of the sensible heat flux. The friction velocity and scaling temperature ratio are related to the Monin-Obukhov length. There is a clear trend with the stability that for a scaling temperature less than 0, the boundary layer is unstable. When the scaling temperature is greater than zero the stability is stable. The exact condition is a relationship based on the friction velocity. Figure 3(b) shows the relationship between the refractive index and the Monin-Obukhov length. The refractive index does not change significantly. However, the structure function coefficient is a turbulent quantity related to the fluctuations of the refractive index and not the magnitude of the refractive index.

The temperature during radiosonde ascents that corresponded to neutrally stable conditions are shown in Fig 4(a). The profiles show a relatively linear decrease in temperature. Temperature changes as the radiosonde exits the boundary layer are not readily observed. The structure function coefficient, C_n^2, is shown in Fig 4(b). A smooth line from sea level to 10,00 meters, the Cn2 profile looked very normal not a whole lot of fluctuations, only what you might see in an error of margin.

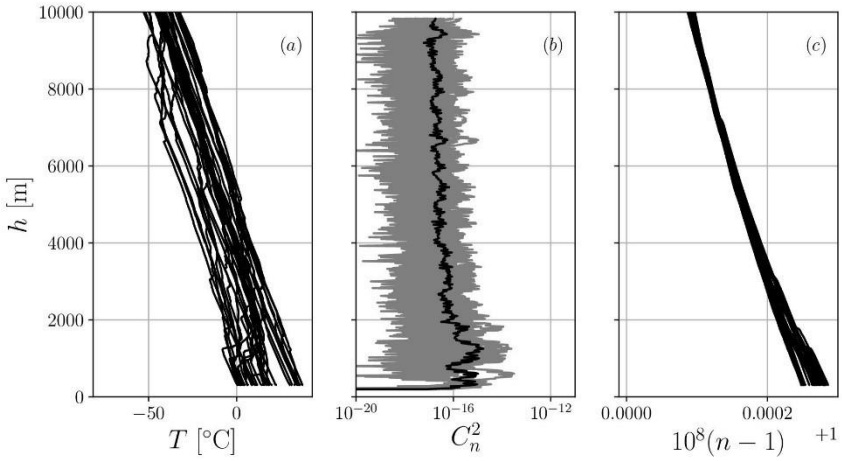

Fig. 4 All radiosonde ascents during neutrally stable conditions. Observations of (a) vertical temperature profile (b) C_n^2 computation and (c) refractive index are shown.

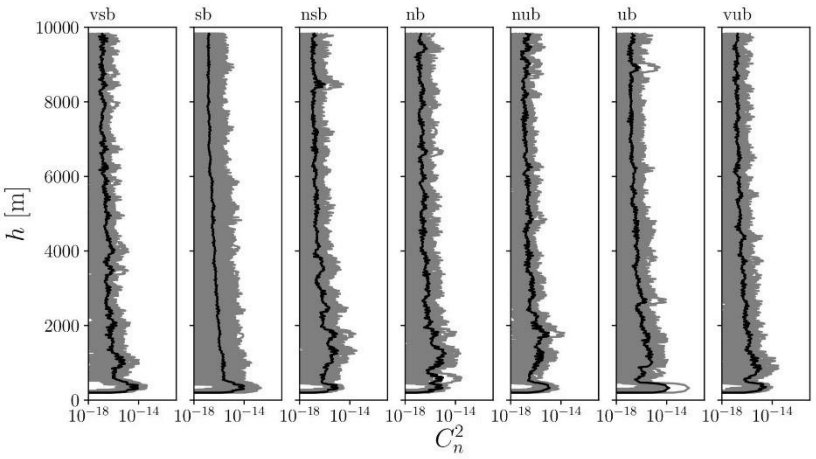

Fig. 5 C_n^2 profiles all radiosonde ascents for all stability conditions. Grey lines are individual radiosonde observations, and the black line is the average C_n^2 profile.

Finally, we wanted to compare all our stability and see if there was a trend developing or was it going to be chaos. From about 250 to a little more than 1000 meters there are stability lines everywhere with no inclination of a pattern. As we progress with height, there is a convergence happening. Around 2000-2200 meters we can see that the stability lines converge, with some disparities at 2500-2800, and at 3000 they all are on top of each other. Here they have crossed the boundary layer where they are no longer under the amount of pressure and exposed to the higher temperatures of ground level. Here we can see that crossing that level does not constrain you as much where the pressures are lower as are the temperatures.

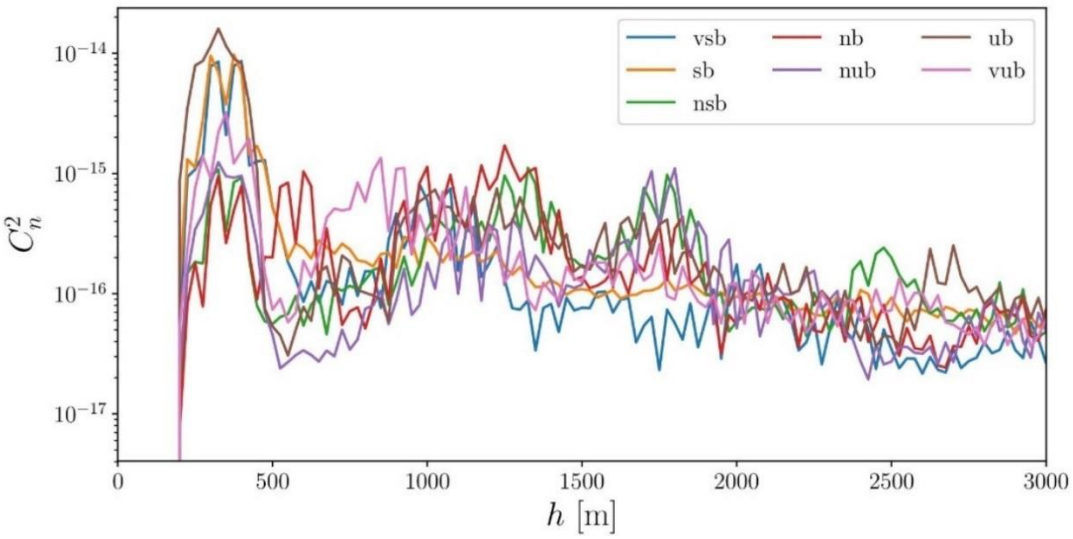

Fig. 6 Average C_n^2 profile for each stability condition.

Fig. 6 shows the compilation of data to show a trend with altitude passing through the boundary layer. Here C_n^2 for all stability groups follow a common average. From this, one can assume that the C_n^2 is nearly independent of the atmosphere's calculated stability. One can calculate the Cn2 profile regardless of windspeed.

VI. Conclusion

The importance of studying optical turbulence is to increase a predictability range suitable to the area or region of interest to the world. Having all the data can help predict how ground-based communication and astronomical observation will be affected. The C_n^2 profiles converge in the upper boundary layer, which lies normally under an altitude of 2000 to 3000 meters. The structure function coefficient does not vary significantly with stability even as the boundary layer height is affected by stability. Once the boundary layer is crossed, no differences are observed based on the stability at the ground.

Acknowledgments

This material is based upon work supported by the U.S. Department of Energy, Office of Science, Office of Biological and Environmental Research, under Award Number DE-SC0023267.

References

[1] Atmospheric Radiation Measurement (ARM) user facility. 2015. Carbon Dioxide Flux Measurement Systems (CO2FLX4M). 2015-07-22 to 2024-02-27, Southern Great Plains (SGP) Central Facility, Lamont, OK (C1). Compiled by A. Koontz, S. Biraud and S. Chan. ARM Data Center. Data set accessed 2024-02-29 at http://dx.doi.org/10.5439/1287574.

[2] Atmospheric Radiation Measurement (ARM) user facility. 2001. Balloon-Borne Sounding System (SONDEWNPN). 2001-04-01 to 2024-02-27, Southern Great Plains (SGP) Central Facility, Lamont, OK (C1). Compiled by E. Keeler, K. Burk, and J. Kyrouac. ARM Data Center. Data set accessed 2024-02-29 at http://dx.doi.org/10.5439/1595321.

[3] Quatresooz, F., Vanhoenacker-Janvier, D., & Oestges, C. (2023). Computation of optical refractive index structure parameter from its statistical definition using radiosonde data. *Radio Science*, *58*, e2022RS007624. https://doi.org/10.1029/2022RS007624